

Permeability-Adjustable Nanocrystalline Flake Ribbon in Customized High-Frequency Magnetic Components

Zhichao Luo ¹, Member, IEEE, Xinru Li ², Student Member, IEEE, Chaoqiang Jiang ³, Member, IEEE, Zongzhen Li, and Teng Long ⁴, Member, IEEE

Abstract—Fe-based nanocrystalline ribbon is an alternative to the ferrite for high-frequency magnetic cores due to its low hysteresis loss and high magnetic saturation. The drawback of the Fe-based nanocrystalline ribbon is its high conductivity. Crushing the homogenous ribbon to restructure a nanocrystalline flake ribbon (NFR) can reduce the conductivity while maintaining other superior magnetic properties of the noncrushed nanocrystalline ribbon. So far, several previous works have proven that the NFR can replace the ferrite in the dual active bridge and wireless power transfer system. However, seldom of these works mention the detailed mechanism of the NFR. In this article, the structure and manufacturing process of the NFR are introduced. The effect of the relative permeability and the crushing pattern on the magnetic properties of NFR has been quantitatively reported. A dual-permeability core formed by two types of NFR has been demonstrated for an inductor. Comparison has been made to inductors using the ferrite core (N27, N87, DMR44) in a similar size. Experiment results show that the dual-permeability NFR core has a lower core loss and higher magnetic saturation than the ferrite counterparts at frequencies from 100 to 300 kHz.

Index Terms—Core loss measurement, high-frequency magnetics, nanocrystalline flake ribbon (NFR), soft magnetic material manufacture.

I. INTRODUCTION

THE power converter is ubiquitous in many modern applications such as electric mobility charging infrastructures,

Manuscript received 12 August 2023; revised 31 October 2023; accepted 2 December 2023. Date of publication 18 December 2023; date of current version 26 January 2024. This work was supported in part by U.K. Engineering and Physical Sciences Research Council under Grant EP/R036799/1, and in part by the Companhia Brasileira de Metalurgia e Mineração under Grant G105565. Recommended for publication by Associate Editor W. Huang. (*Corresponding author: Teng Long.*)

Zhichao Luo is with the Department of Engineering, University of Cambridge, CB3 0FA Cambridge, U.K., and also with the School of Electric Power Engineering, South China University of Technology, Guangzhou 510640, China (e-mail: hgzcsluo@scut.edu.cn).

Xinru Li and Teng Long are with the Department of Engineering, University of Cambridge, CB3 0FA Cambridge, U.K. (e-mail: xl418@cam.ac.uk; tl322@cam.ac.uk).

Chaoqiang Jiang is with the Department of Electrical Engineering and the State Key Laboratory of Terahertz and Millimeter Waves, City University of Hong Kong, Kowloon, Hong Kong (e-mail: chjiang@cityu.edu.hk).

Zongzhen Li is with Jiangsu JITRI Advanced Energy Materials Research Institute Company, Ltd., Changzhou, China (e-mail: zongzhenli@hotmail.com).

clean energy storage systems, and mega data centers [1], [2], [3], [4]. Power density is one of the most significant factors when designing the power converter and the magnetic component. Enormous efforts have been made in the advanced structures of the magnetic core for various applications, such as the power factor correction converter inductor with quasi-distributed gaps core [5], the distributed ferrite cores structure in the wireless power transfer system (WPT) for capsule robots [6], leakage flux shield ferrite layer for the 11 kW WPT system [7], and the magnetized capacitance analysis of inductors with ferrite cores [8].

Most of the efforts were made on ferrite cores with a low magnetic saturation point between 0.2 and 0.5 T [9], [10] and high mechanical brittleness [11]. The Fe–Cu–Nb–Si–B nanocrystalline soft magnetic material is a suitable alternative for ferrite owing to its high magnetic saturation, low hysteresis loss, and high Curie temperature (550 °C). Fe-based nanocrystalline soft magnetic alloys are increasingly popular in electromagnetic compatibility filters, motors, transformers, wireless charging, and a variety of others [12], [13], [14], [15].

The nanocrystalline ribbons are typically laminated along the transverse direction to reduce the eddy current loss caused by the main flux at the longitudinal direction. However, the high relative permeability of the nanocrystalline ribbon requires a discrete core air gap for most applications, leading to substantial eddy current losses [16] and copper loss at high frequencies [17]. Recently, a novel reconstructive crushing process has been applied after the nanocrystalline ribbon is laminated with the polyester release film. The relatively brittle nanocrystalline ribbon is crushed into fine flakes on a scale of 50–200 μm and bonded on the film surface [18]. The binder (silicone, acrylic, polyisobutylene, and rubber based pressure sensitive adhesives) between flakes effectively becomes distributed micro air gaps. Therefore, the induced eddy current loop on the surface of the nanocrystalline flake ribbon (NFR) can be effectively reduced and the relative permeability can be controlled to be from 800 to 3300 by the crushing process.

In [19], the characterization of the NFR cylinder core is conducted under different magnetic field excitations and temperatures. Besides, some previous works have adopted the NFR in the high-frequency magnetic component design. In [18], the NFR is used in the dual active bridge transformer core to achieve higher efficiency than the ferrite N87 core. In [11], the NFR is used as the magnetic shield in the 11 kW WPT system to

improve the system's power density. In [20], the combined ferrite and NFR shield is proposed to achieve better magnetic shielding effectiveness. However, the impact of the crushing process on the electromagnetic and loss characteristics of NFR remains unknown. The benefits and applications of the simple manufacturing process of customized cores enabled by NFR have not been explored. This article aims to reveal the effect of the crushing process to alter the NFR properties and demonstrate that high-frequency magnetic cores can be designed and built by the user-defined NFR material and core shapes for improved performance.

Multipermeability core can achieve a uniform B-field distribution inside the core, which avoids the partial magnetic saturation issue and reduces the core loss. The ferrite tapes with different μ_r were applied to build the multipermeability cores of the planar inductor and low-temperature cofired ceramic inductor [21], [22]. The ferrite noise suppression sheets with different μ_r were applied as the inductor core in the high-frequency dc/dc converter [23]. In [24] and [25], the multipermeability ferrite cores were fabricated by the multiextruder paste extrusion three-dimensional printer and the gradient sintering technology, respectively. However, the above multipermeability cores are suitable for the low power and low magnetic flux density applications due to the low relative permeability and low magnetic saturation of the ferrite powder core. Making such ferrite, LTCC, or powder multipermeability cores requires special equipment with high energy. The multipermeability core made by NFR can offer a new option for high-power inductive component design due to its relatively high μ_r and magnetic saturation. Making the multipermeability NFR cores does not involve high energy (temperature or pressure) process. The NFR has a ribbon format which can be stacked, laminated, or wound with or without thin film substrates. The shape and size of the NFR cores can be altered based on specific requirements and the relative permeability of the NFR can be adjusted by the crushing process. NFR can offer a unique option for inductive component design in terms of relative permeability and magnetic saturation as presented in [18]. These features and design freedom offer versatile inductive core design by the end user without high energy process.

The main contributions of this article are listed as follows.

- 1) The effect of the crushing process on the magnetic properties of NFR is revealed and the mechanism behind the phenomena is discussed.
- 2) Different crushing patterns and their associated impacts on the magnetic properties of NFR are discussed.
- 3) A dual-permeability inductor based on NFR is built and compared to other ferrite cores with the similar size in order to prove the core loss advantage of the NFR.

The main goal of this article is to provide the power electronics engineer with the knowledge of choosing and making the proper structure of the NFR in the magnetic component design.

The rest of this article is organized as follows. In Section II, the development of the Fe-based nanocrystalline ribbon and flake ribbon is introduced including the manufacturing process. In Section III, the core loss measurement method and the excitation circuit are presented. In Section IV, the effect of the crushing process on the magnetic properties of NFR is investigated. In Section V, the dual-permeability inductor based on NFR is built

and compared to three other ferrite cores to verify the efficiency advantage of the NFR core. Finally, the conclusion is drawn in Section VI.

II. DEVELOPMENT OF FE-BASED NANOCRYSTALLINE RIBBON

The Fe-based nanocrystalline soft magnetic material is the FeBSiNbCu composition discovered by Yoshizawa and Herzer in 1988 and 1989 [26], [27], respectively. The chemistry of such alloy is unique as it allows for the material to be cast fully amorphous followed by a heat treatment above the onset crystallization temperature to set the nanocrystalline phase. The Cu content tends to promote nucleation, and the Nb content tends to slow grain growth. The nucleation and growth kinetics are then controlled such that the partial crystallization process can be done slowly in a conventional furnace [28].

As shown in Fig. 1 stage I, the amorphous ribbons with a nominal composition of $\text{Fe}_{73.5}\text{Cu}_1\text{Nb}_3\text{Si}_{15.5}\text{B}_7$ is annealed at 550 °C in the inert gas atmosphere (N_2 or Ar) to achieve the nanocrystalline state. Yoshizawa, the researcher from Hitachi Metals, Co., Ltd, found that if a magnetic field is applied during the annealing, the squareness of the B–H curve can be controlled. As presented in Fig. 1 stage I, a circumferential direction magnetic field results in the high squareness of the B–H curve, while a vertical magnetic field to the core plane leads to the low squareness of the B–H curve. If there is no magnetic field during annealing, the medium squareness is achieved. Different types of B–H curves correspond to different applications. For example, the high squareness nanocrystalline can be used as the pulsed power core which is suitable for saturable cores and step-up pulse transformer cores that are used in high-voltage pulsed power supplies. The medium squareness nanocrystalline exhibits excellent magnetic properties, such as low core loss and high magnetic saturation, compared to Mn–Zn ferrite at high frequency [29]. Thus, it can be used as the core in the transformer and inductor for the power converters operating at hundreds of kHz. And the medium squareness nanocrystalline is the most widely applied in the market among those three types of nanocrystalline material.

New Fe-based nanocrystalline compositions have been developing for recent years and appear to be on the verge of commercialization in many cases. For example, the Co- and FeNi-based alloys are reported to have a better mechanical property than the conventional nanocrystalline alloys with similar saturation induction levels [30]. Some researchers also found that the saturation induction level can be increased above the Fe-based amorphous by maximizing the Fe content while minimizing Nb [28].

As shown in Fig. 1 stage II, the nanocrystalline ribbon is stuck by two polyester release films with the dielectric adhesive layer on both sides. Then, the nanocrystalline ribbon with the protective polyester films is crushed into fine flakes in 50 to 200 μm size. A compression process is applied and the adhesives fill the gaps between the flakes with dielectric adhesives afterward. Due to the crushing and compression process, both the conductivity and relative permeability of the NFR are reduced. The eddy current loss caused by the fringing flux normally vertical enters the ribbon plane is significantly decreased. The reduced permeability allows high magnetic field for high power

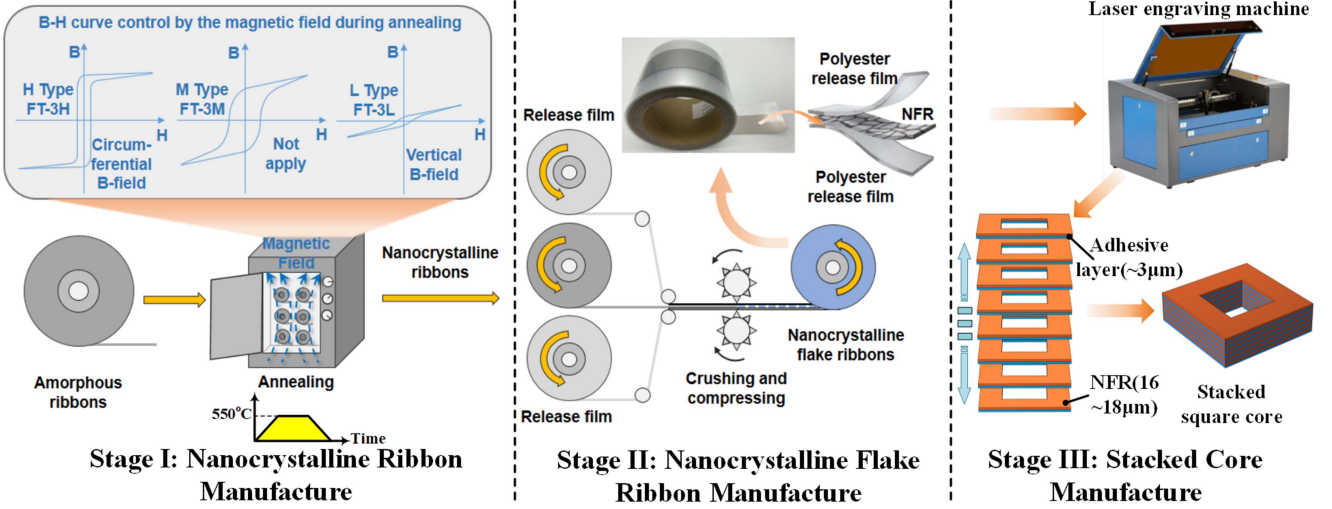


Fig. 1 Manufacturing process of the NFR stacked core.

applications to avoid saturation. The crushing process is the vital stage for fabrication of the NFR. The pressure and pattern of the crushing process can affect the electromagnetic properties such as the relative permeability and core loss, which will be discussed in detail in Section IV.

In Fig. 1 stage III, the stacked NFR core manufacturing process is presented. A laser engraving machine is used to achieve the NFR core with the customized geometry (square core with a square hole in this article) to have clean cutting edge of sandwiched thin NFR and release films. According to the lab test, a 39 W laser beam is sufficient to penetrate the NFR with the polyester release film. If the release film is relatively thick, e.g., more than 10 μm considering only 18 μm thickness of the NFR, the polyester release film should be peeled off to ensure a decent stacking factor. And the multiple layers of NFR with the customized shape are stacked together by the dielectric adhesive layer which is normally 3–5 μm . The film can also be retained if it is relatively thin. Multiple NFRs from different crushing processes can be combined into a same core from this process to achieve a multipermeability core because the core geometry and electromagnetic properties are accessible for power electronics engineers since no high-temperature or high-pressure procedure is needed on stage III.

III. CORE LOSS MEASUREMENT METHOD AND CIRCUIT DESIGN

The *LCL* resonant circuit topology is used in this article to provide the core under test (CUT) with the ac sinusoidal excitation. As shown in Fig. 2, the *LCL* resonant circuit is fed by a full-bridge inverter. L_{f1} and C_{f1} are the compensation inductor and capacitor in the *LCL* resonant tank, respectively. The resonant condition is presented as follows:

$$\omega_0 L_{eq} = \omega_0 L_{f1} = 1/\omega_0 C_{f1}. \quad (1)$$

In [19], our previous work has proved that the *LCL* resonant circuit is able to suppress the high-order harmonics of the excitation current against the capacitance C_{f1} deviation even

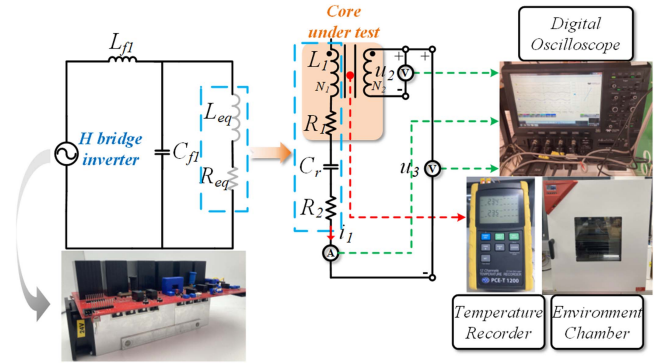


Fig. 2. *LCL* AC resonant test circuit for core loss density measurement.

when the equivalent quality factor ($Q = \omega_0 L_{eq}/R_{eq}$) is low compared to the *LC* resonant circuit proposed in [9].

The numbers of turns on the primary and secondary windings in the CUT are N_1 and N_2 , respectively. L_1 and R_1 are the self-inductance and parasitic resistance of the primary winding, while the open-circuit voltage u_2 of the secondary winding is measured. Since there is a nearly 90° phase difference between the excitation current in the primary winding, i_1 , and the induced voltage across the secondary winding u_2 , minor phase desynchrony between the voltage and current probes in the oscilloscope will lead to considerable measurement error of the core loss. Therefore, an additional capacitor C_r is used to reduce the phase difference between u_3 and i_1 such that the power loss measurement could be more robust.

According to paper [31], the capacitance of C_r is calculated by

$$C_r = \frac{N_1}{N_2(2\pi f)^2 L_1} \quad (2)$$

where f is the operating frequency.

And the core loss can be obtained by

$$P_C = f \cdot \frac{N_1}{N_2} \int_0^{1/f} i_1(t) \cdot u_3(t) dt - i_1^2 R_2. \quad (3)$$

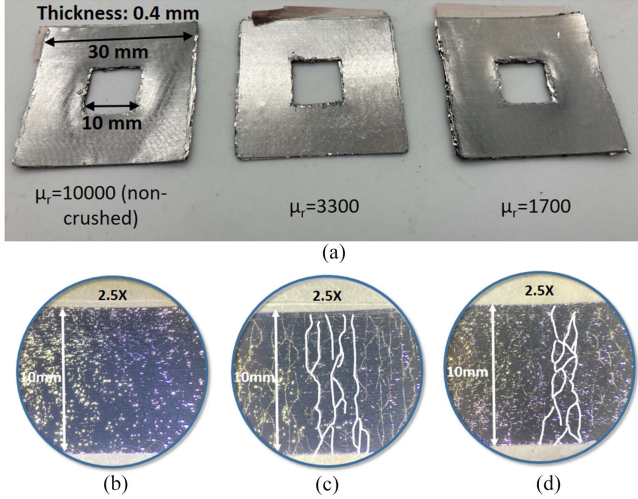


Fig. 3. (a) Fe-based nanocrystalline cores with different relative permeability. (b) 2.5X magnification view of the NFR with $\mu_r = 10\,000$ and (c) with $\mu_r = 3300$ and (d) with $\mu_r = 1700$. (Part of the cracks are highlighted. White spots are due to light reflection.)

As shown in Fig. 2, a Lecroy MDA 810A digital oscilloscope is used to measure u_2 , u_3 , and i_1 . The core temperature is controlled by the BINDER environment chamber and recorded by the PCT-E 1200 temperature recorder.

IV. CRUSHING EFFECT ON THE MAGNETIC PROPERTIES OF NFR

A. Relative Permeability

Three cores with the same dimension stacked by NFRs with different relative permeabilities were built as shown in Fig. 3. The NFRs are provided by Proterial *Ltd.*, (former Hitachi Metal *Ltd.*). The manufacturing process of the NFR core is illustrated in Fig. 1. A single NFR layer can be cut to a square with a square hole. The cutting edge is uneven because some nanocrystalline flakes on the edge stick to spilled adhesive which is caused by expansion from high temperature during the laser cutting. Then, the NFR core is built by stacking multiple customized NFR layers together. Apart from stacking, the NFR cores can also be built in the form of a wound core.

The core with $\mu_r = 10\,000$ uses a noncrushed nanocrystalline ribbon. The outer and inner dimensions of the core are $30\text{ mm} \times 30\text{ mm}$ and $10\text{ mm} \times 10\text{ mm}$, respectively. The core was made of 20-layer ribbons and the total thickness is 0.4 mm. The other two cores were made of 20 layers of NFR too. These two cores have different relative permeabilities because the flake size of each ribbon is different. The NFR with the larger individual flakes has a higher μ_r and a higher conductivity as shown in Fig. 3, in which Fig. 3(b) shows no crushed flakes, while a few cracks are visible in Fig. 3(c) and (d). The flake size in Fig. 3(c) is larger than that in Fig. 3(d).

The core loss under different peak magnetic flux densities is shown in Fig. 4(a). It is observed that the crushed ribbon, i.e., the NFR exhibits higher core losses. This phenomenon seems nonintuitive as the crushing process is motivated to have a lower core loss because flakes breakdown the eddy current loops

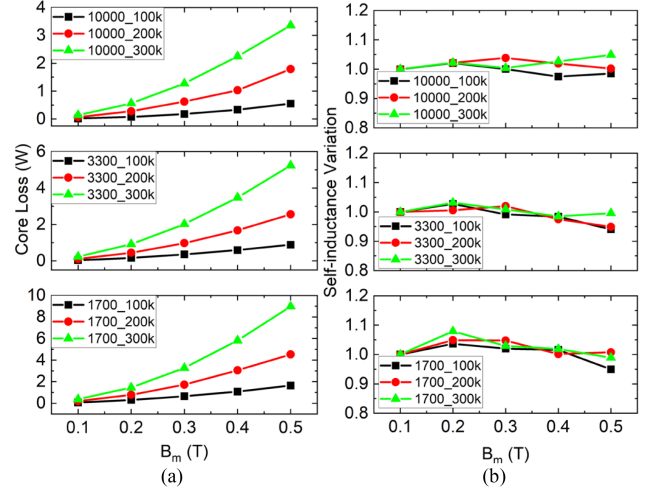


Fig. 4. (a) Crushing impact on the core loss at 25 °C. (b) Self-inductance variation for the inductors using different μ_r cores.

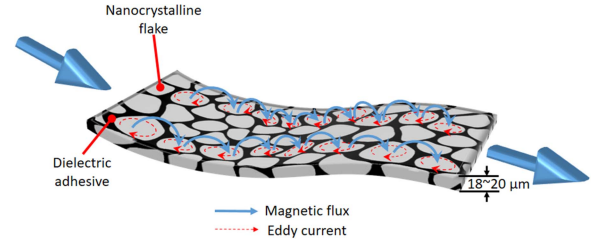


Fig. 5 Conceptual magnetic flux path inside the NFR.

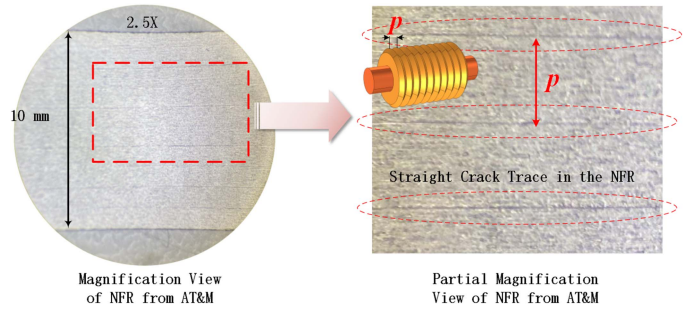


Fig. 6. 2.5X magnification view of the NFR made by AT&M.

caused by the external fringing flux which enters the surface of the ribbon. However, the flakes and micro air gaps have caused another fringing flux oriented from the mainstream flux aligning with the ribbon direction. As shown in Fig. 5, when the magnetic flux flows are along the longitudinal direction of the ribbon, the magnetic flux will bounce from one flake to another due to the dielectric adhesive between them. This bouncing flux effectively becomes fringing flux with nonzero vertical component entering the surfaces of small flakes, which results in higher eddy current loss in the ribbon. In a practical magnetic core made by multiple stacked NFR layers, the bouncing magnetic flux of any one layer can also cause eddy current loops in the flakes of its adjacent layers. Reduced relative permeability will result in a finer flake size. As shown in Fig. 4(a), the core loss of the NFR@ μ_r 3300 is around 50%–60% higher than that of the noncrushed one. The

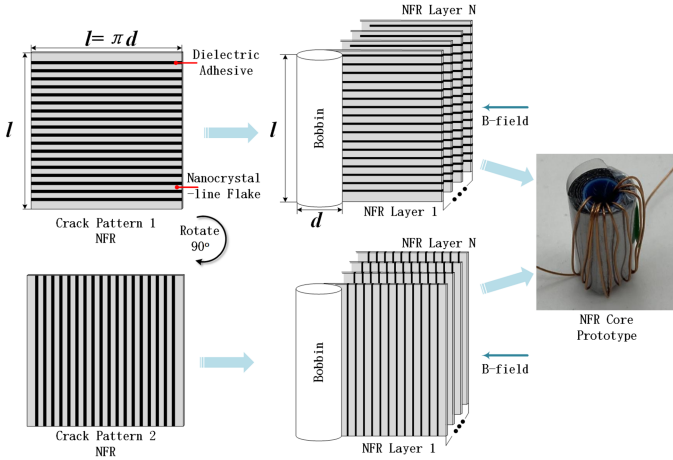


Fig. 7. Structure demonstration of different crushing pattern NFR cores.

core loss of the NFR at $\mu_r 1700$ is around 160%–170% higher than that of the noncrushed one.

It is worth noting that the increased core loss is caused by the main flux instead of fringing flux since no discrete air gap presents. Eddy current loss reduction from fringing flux is still reduced by micro air gaps at each layer.

The relative permeability variation with respect to the peak value of the B-field excitation (B_m) is an important factor to consider when designing a magnetic component as it is a straightforward inductor to show whether the magnetic core suffers from magnetic saturation or not. If the self-inductance decreases more than 20% of its nominal value under a specific B_m , the core begins to saturate. In order to investigate the impact of the crushing level on the magnetic saturation, the self-inductance variation (ΔL) is used, which is defined as follows:

$$\Delta L = \frac{L}{L(0.1T)} \quad (4)$$

where $L(0.1T)$ is the self-inductance of the inductor under $B_m = 0.1 T$.

As presented in Fig. 4(b), the self-inductance variation is within $\pm 8\%$ in all three cores when B_m is increased to 0.5 T and f varies from 100 to 300 kHz. This suggests that the flake size inside the NFR core has a minor effect on the magnetic saturation. Adjustable permeability and high magnetic saturation point make NFR suitable for a gapless core. The winding and core loss caused by discrete air gaps can be significantly reduced [17], [32].

B. Crushing Pattern

As highlighted by the dashed circle in Fig. 6, the crushing pattern of the NFR provided by AT&M Ltd has the longitudinal direction of cracks along the ribbon running direction. This crushing pattern can be fabricated by the circumferentially slotted roller as shown in Fig. 6.

This ribbon was wound in two different directions to enable the main magnetic flux inside these two cores flowing in parallel and perpendicular to the cracks, respectively. As shown in Fig. 7, the NFR was cut as a square layer and then wound onto a cylindrical bobbin with the dimension of $\emptyset 6 \text{ mm} \times 20 \text{ mm}$ to

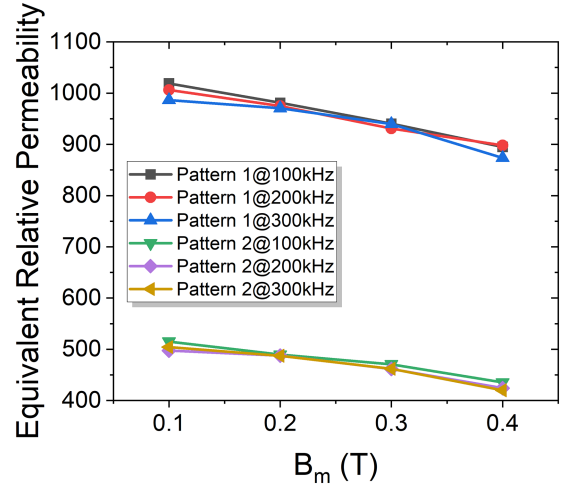


Fig. 8. Crushing pattern effect on the equivalent relative permeability.

build the NFR core (Pattern 1). Then, the same NFR square layer was rotated 90° (Pattern 2) so that the crack's orientation is changed with respect to the B-field. The equivalent relative permeability is obtained by the following equation:

$$\mu_{r_eq} = \frac{Ll_e}{\mu_0 N^2 A} \quad (5)$$

where l_e is the effective magnetic flux loop of the cylinder core, A is the cross-sectional area of the core, N is the number of turns, μ_0 is the permeability of the free space, and L is the self-inductance of the inductor obtained by the experiment measurement.

According to the results shown in Fig. 8, the crushing pattern has a considerable effect on the equivalent relative permeability. The equivalent relative permeability of the Pattern 2 core is reduced by 50% compared to that of Pattern 1 core. This is attributed to the perpendicular encounter to the cracks of the main magnetic flux, causing mostly effective interruption of flux so does reduce the relative permeability.

As B_m increases, μ_{r_eq} of both two patterns has a similar decrease tendency and the drop is around 10% when B_m varies from 0.1 to 0.4 T. This suggests that different crushing patterns do not have an evident impact on the magnetic saturation of the NFR.

Fig. 9 shows the core loss comparison between two crushing patterns. When the operating frequency is 100 kHz, there is a minor core loss difference between two patterns. As the operating frequency increases to 200 and 300 kHz, the core loss of Pattern 2 becomes higher than that of Pattern 1.

According to Bertotti's core loss separation theory [33], the total core loss P_c consists of hysteresis loss P_h , eddy current loss P_e , and excess loss P_{ex} , of which the P_{ex} is much smaller than the other two terms [34]. The general core loss calculation equation is shown as follows:

$$\begin{aligned} P_c &= P_h + P_e + P_{ex} \\ &= k_h f B_m^\beta + k_e (f B_m)^2 + k_{ex} (f B_m)^{1.5} \end{aligned} \quad (6)$$

where k_h , k_e , k_{ex} , and β are the undetermined constants.

If the core loss per magnetization cycle is used, the hysteresis energy loss density per magnetization cycle is independent of

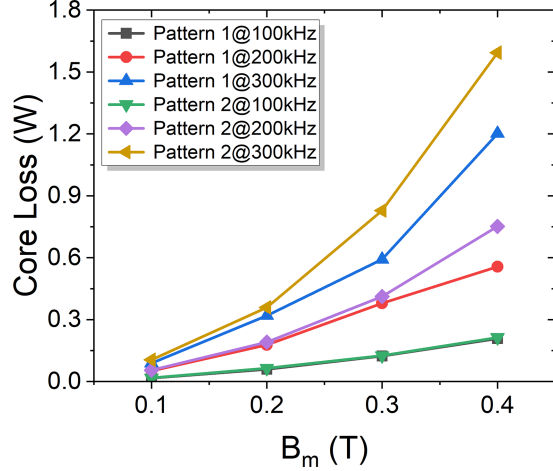


Fig. 9. Crushing pattern effect on the core loss at 25 °C.

TABLE I
VARIATION OF ENERGY LOSS DENSITY PER MAGNETIZATION CYCLE

| Peak magnetic flux density | λ @Crushing pattern 1 | λ @Crushing pattern 2 |
|----------------------------|-------------------------------|-------------------------------|
| $B_m = 0.1$ T | 0.81 | 1 |
| $B_m = 0.2$ T | 0.79 | 0.86 |
| $B_m = 0.3$ T | 0.59 | 1.21 |
| $B_m = 0.4$ T | 0.93 | 1.49 |

frequency as presented in the following:

$$Q_c = \frac{P_c}{f} = Q_h + Q_e + Q_{ex} = k_h B_m^\beta + k_e f B_m^2 + k_{ex} f^{0.5} B_m^{1.5}. \quad (7)$$

Then, define the variation of the energy loss density per magnetization cycle as follows:

$$\lambda = \frac{Q_{c_300\text{kHz}} - Q_{c_100\text{kHz}}}{Q_{c_100\text{kHz}}} \quad (8)$$

where $Q_{c_100\text{kHz}}$ and $Q_{c_300\text{kHz}}$ is the energy loss density per magnetization cycle when f is 100 and 300 kHz, respectively.

The portion of eddy current energy loss can be analyzed qualitatively. For example, if the hysteresis loss is dominant in the total core loss, λ is close to 0. The higher λ is, the higher portion of eddy current loss will be. As presented in Table I, λ of two different crushing patterns under different B_m is calculated. λ of the crushing pattern 2 is higher than that of the crushing pattern 1 for all different B_m . This infers that the eddy current loss in the crushing pattern 2 is more significant than that in the crushing pattern 1.

Overall, the effect of the crushing process on the magnetic properties of the NFR can be summarized.

- 1) Lower relative permeability means a larger micro distributed air gap inside the core and leads to a higher core loss but negligible effect on the magnetic saturation.
- 2) The orthogonal crack direction against the main flux results in more reduction in the relative permeability and increase of the eddy current loss.

TABLE II
DESIGN PARAMETERS OF THE INDUCTORS

| Parameters | N27 | N87 | DMR44 | NFR |
|--------------------------------|--------------------|--------------------|--------------------|--------------------|
| Inner diameter/ side length | 15 mm | 15 mm | 15 mm | 8 mm |
| Outer diameter/ side length | 25 mm | 25 mm | 25 mm | 20 mm |
| Height | 10 mm | 10 mm | 2 mm | 2 mm |
| Relative permeability | 2200 | 2200 | 2200 | 3000/1580 |
| Cross-section area | 50 mm ² | 50 mm ² | 10 mm ² | 12 mm ² |
| Effective magnetic path length | 62.8 mm | 62.8 mm | 62.8 mm | 56 mm |
| Number of turns | 5 | 5 | 5 | 5 |
| Self-inductance | 56.4 μ H | 59.2 μ H | 12.1 μ H | 12.7 μ H |

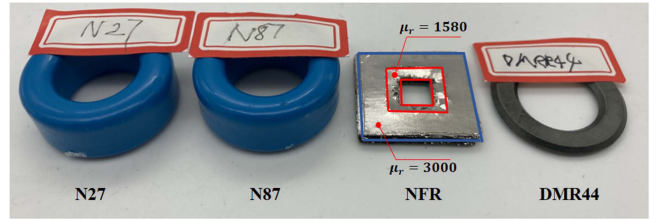


Fig. 10. Core prototypes in the experiment.

V. PERFORMANCE COMPARISON BETWEEN THE NFR CORE AND THE FERRITE CORE

In this section, a multipermeability NFR core was built and compared to three other ferrite cores, namely N27, N87 (from TDK), and DMR44 (from DMEGC) in a similar size. The inductors using those cores have approximately the same self-inductance with the same number of turns as presented in Table II. Taking the advantage of the flexibility of the NFR, customized magnetic cores can be proceeded in a straightforward course, without involving high temperature or high pressure process. As shown in Fig. 10, the NFR core purposely includes two subcores with different relative permeabilities. The relative permeabilities of the outer and inner subcores are 3000 and 1580 at 200 kHz. The combination of two permeabilities results in a more homogenous B-field distribution inside the core [25].

For the sake of handmade fabrication, the square core is built instead of the toroid core. The per unit thickness inductance of the square core can be expressed by

$$dL = N^2 \frac{\mu_0 \mu_r h d l_h}{8 l_h} \quad (9)$$

where h is the height of the core and l_h is half of the corresponding side length of the core.

For the dual-permeability square core, the total self-inductance can be calculated by

$$\begin{aligned} L_{\text{tot}} &= N^2 \frac{\mu_0 \mu_i h}{8} \int_{l_1/2}^{l_2/2} \frac{1}{l_h} d l_h + N^2 \frac{\mu_0 \mu_o h}{8} \int_{l_3/2}^{l_4/2} \frac{1}{l_h} d l_h \\ &= N^2 \frac{\mu_0 \mu_i h}{8} \left(\ln \frac{l_2}{2} - \ln \frac{l_1}{2} \right) + N^2 \frac{\mu_0 \mu_o h}{8} \left(\ln \frac{l_4}{2} - \ln \frac{l_3}{2} \right) \end{aligned} \quad (10)$$

where μ_i, μ_o are the relative permeabilities of the inner and outer subcores; l_1, l_2 are the inner and outer side lengths of the inner subcore, while l_3, l_4 are the inner and outer side lengths of the outer subcore. According to (10), l_1, l_2, l_3, l_4 are 8, 11, 11.5, and 20 mm in order to obtain the similar self-inductance as the inductor with DMR44 ferrite core. The 0.5 mm gap between l_2 and l_3 is the margin for the laser cutter manufacture error. Due to the commercial cores availability, two 10-mm height ferrite cores, N27 and N87, are used in this experiment. The inner and outer diameters of these two cores are the same as the DMR44 core. Since the magnetic field inside the core is homogeneously distributed along the height direction, the core loss of the 2-mm height core is approximately one-fifth of that of the 10-mm height core. Therefore, the core losses of N87 and N27 in Fig. 11 are one-fifth of the original experiment measurement.

The core loss comparison is presented in Fig. 11(a)–(c) under three different operating frequencies. The ambient temperature was controlled at 80 °C as the optimal operating temperature for ferrite cores. The ferrite cores suffer from magnetic saturation when the excitation current is higher than 0.55 A. The inner subcore, under higher H-field excitation, has lower relative permeability. Thus, the inductor using the NFR core is able to operate under 1.8 A without being saturated.

The zoom-in views from 0 to 0.55 A at different frequencies are also presented in Fig. 11. Three ferrite cores have the similar core loss but the NFR core has the lowest core loss among all of the study cases. For example, when the excitation current is around 0.3 A, the loss of NFR is 57.3%, 56.4%, and 56% lower than that of DMR44 at 100, 200, and 300 kHz, respectively.

Furthermore, the thermal analysis is conducted with the 0.3 A excitation for the NFR and DMR44 cores. The ambient temperature is 25 °C in the lab. The thermal images are captured by using the FLIR thermal camera E53 when the cores reach to the temperature equilibrium. As shown in Fig. 12, the NFR core has a lower equilibrium temperature at three different operating frequencies compared to the DMR44 ferrite core. At 300 kHz, the DMR44 core reaches 107 °C which is not an optimal operating temperature for ferrite. Therefore, it can be concluded that the NFR core has superior magnetic properties in terms of core loss and magnetic saturation compared to the ferrite core of a similar size.

The self-inductance variation of the inductor made by four different cores is compared under dc bias. In this test, the pulse voltage excitation (V_{dc}) is provided to the inductor and the inductor current is measured. Then, the self-inductance can be calculated by $V_{dc}/(di/dt)$. As shown in Fig. 13, the self-inductance of the ferrite cores starts to decrease when the magnetic field strength is from 80 to 200 A/m. In contrast, the self-inductance of the NFR core drops only when the magnetic field strength is higher than 250 A/m showing a stable self-inductance under the large dc magnetic field. Thus, the NFR core is capable of maintaining a stable self-inductance under the large dc magnetic field.

VI. CONCLUSION

In this article, the manufacturing process of the NFR core was introduced. The relative permeability and conductivity of the NFR are mainly determined by the crushing pressure, ribbon winding tension, and crushing pattern. The effect of the crushing

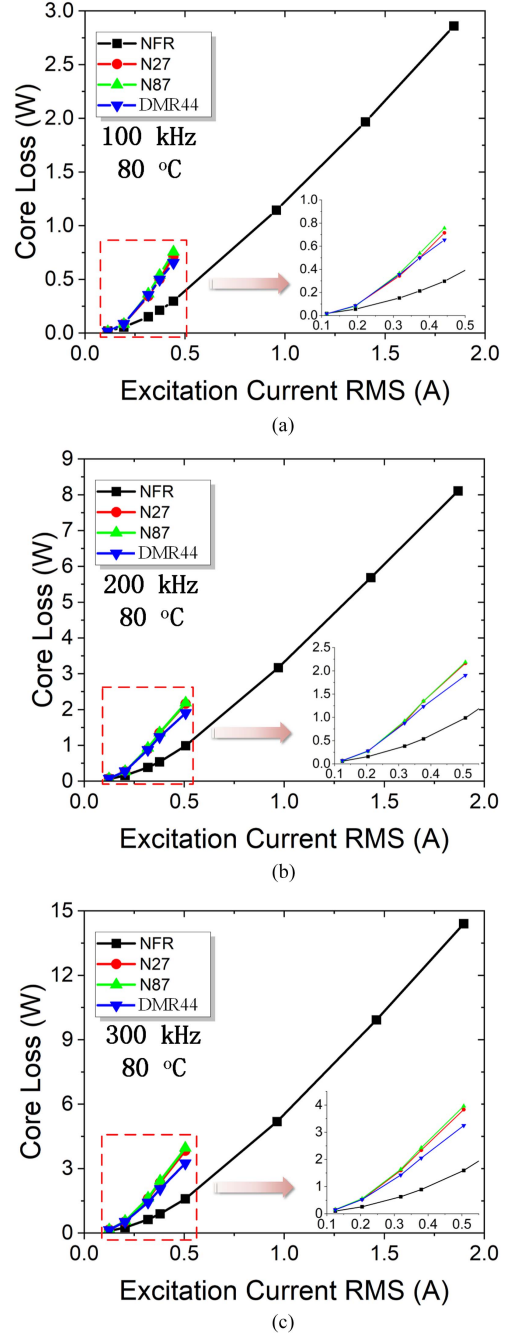


Fig. 11. Core loss comparison at three different frequencies. (a) 100 kHz. (b) 200 kHz. (c) 300 kHz.

level and crushing pattern on the magnetic properties of NFR is studied from 100 to 300 kHz excitation. This frequency range covers many of the resonant power converter applications. The experiment results show that the crushing level of the NFR increases the core loss due to more tiny eddy current loops in the flakes. But it has a minor effect on the magnetic saturation threshold. Two cylinder cores with different crushing patterns are made in order to investigate their effect on the magnetic properties of NFR. Based on the experiment measurement, if the cracks in the ribbon hinder the main magnetic flux inside the core, it leads to a relative permeability drop and a core loss increase.

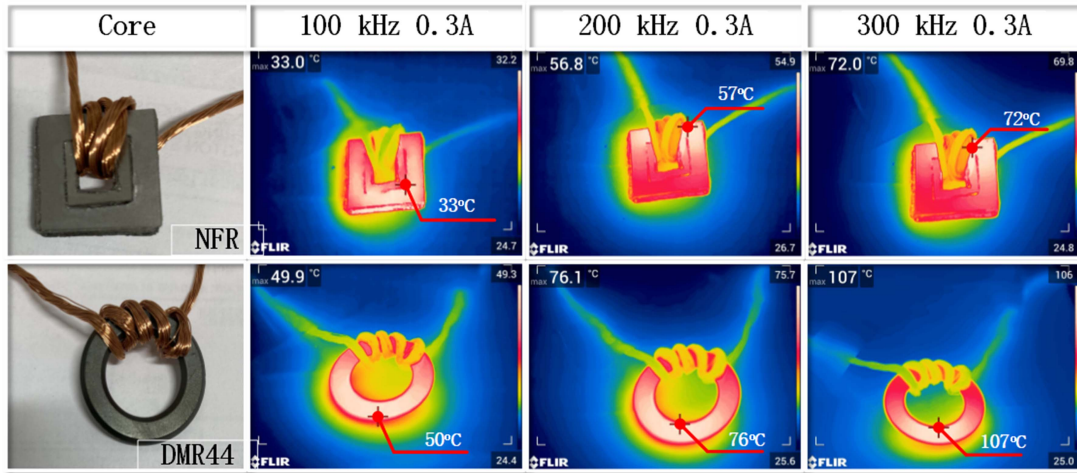


Fig. 12. Thermal images of the NFR and DMR44 cores at different operating frequencies.

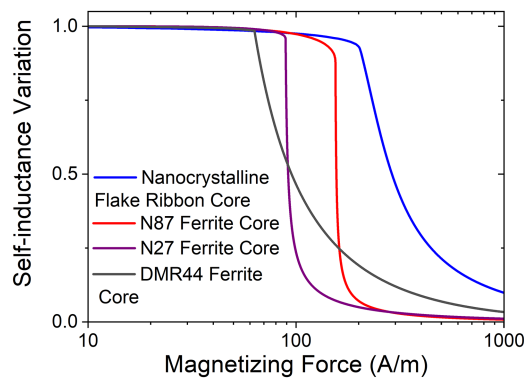


Fig. 13. Self-inductance variation comparison under DC bias.

Finally, the dual-permeability NFR core is built to conduct a comparison experiment with three other ferrite cores of a similar size. Experiment results show that the dual-permeability NFR core has a lower core loss, a higher magnetic saturation, and the high consistency of self-inductance under the large dc bias excitation.

Compared to the powder cores [9], the NFR proposed has higher relative permeability and can be designed into a customized core shape due to NFR's ribbon format and flexibility. However, the powder core can be regarded as an isotropy material, while the core formed by the NFR is the anisotropy material, which will be a challenge for estimating the core loss. The accurate core loss prediction model for the NFR core will be the focus of the authors' future work.

REFERENCES

- [1] H. Tu, H. Feng, S. Srdic, and S. Lukic, "Extreme Fast charging of electric vehicles: A technology overview," *IEEE Trans. Transport. Electric.*, vol. 5, no. 4, pp. 861–878, Dec. 2019.
- [2] Y. Cui, F. Yang, L. M. Tolbert, D. J. Costinett, F. Wang, and B. J. Blalock, "Load-dependent soft-switching method of half-bridge current doubler for high-voltage point-of-Load converter in data center power supplies," *IEEE Trans. Power Electron.*, vol. 32, no. 4, pp. 2925–2938, Apr. 2017.
- [3] R. Barzegarkhoo, M. Forouzesh, S. S. Lee, F. Blaabjerg, and Y. P. Siwakoti, "Switched-capacitor multilevel inverters: A comprehensive review," *IEEE Trans. Power Electron.*, vol. 37, no. 9, pp. 11209–11243, Sep. 2022.
- [4] Z. Meng, X. Xia, R. Xu, W. Liu, and J. Ma, "HYDRO-3D: Hybrid object detection and tracking for cooperative perception using 3D LiDAR," *IEEE Trans. Intell. Veh.*, vol. 8, no. 8, pp. 4069–4080, Aug. 2023.
- [5] R. S. Yang, A. J. Hanson, C. R. Sullivan, and D. J. Perreault, "Design flexibility of a modular low-loss high-frequency inductor structure," *IEEE Trans. Power Electron.*, vol. 36, no. 11, pp. 13013–13024, Nov. 2021.
- [6] H. Zhuang, W. Wang, K. Zhao, S. Kuang, Z. Wang, and G. Yan, "Efficient power receiving coil with novel ferrite core structure for capsule robot," *IEEE Trans Biomed. Circuits Syst.*, vol. 16, no. 5, pp. 939–946, Oct. 2022.
- [7] M. Mohammad, O. C. Onar, V. P. Galigekere, G.-J. Su, and J. Wilkins, "Magnetic shield design for the double-D coil-based wireless charging system," *IEEE Trans. Power Electron.*, vol. 37, no. 12, pp. 15740–15752, Dec. 2022.
- [8] R. R. Zhang, S. Wang, T. Long, J. Qiu, K. F. Liu, and H. Zhao, "The magnetized capacitance, first resonant frequency, and electromagnetic analysis of inductors with ferrite cores," *IEEE Trans. Ind. Electron.*, early access, Jul. 25, 2023, doi: [10.1109/TIE.2023.3294611](https://doi.org/10.1109/TIE.2023.3294611).
- [9] C. Jiang, X. Li, S. S. Ghosh, H. Zhao, Y. Shen, and T. Long, "Nanocrystalline powder cores for high-power high-frequency applications," *IEEE Trans. Power Electron.*, vol. 35, no. 10, pp. 10821–10830, Oct. 2020.
- [10] Z. Luo and X. Wei, "Analysis of square and circular planar spiral coils in wireless power transfer system for electric vehicles," *IEEE Trans. Ind. Electron.*, vol. 65, no. 1, pp. 331–341, Jan. 2018.
- [11] M. Xiong, X. Wei, Y. Huang, Z. Luo, and H. Dai, "Research on novel flexible high-saturation nanocrystalline cores for wireless charging systems of electric vehicles," *IEEE Trans. Ind. Electron.*, vol. 68, no. 9, pp. 8310–8320, Sep. 2021.
- [12] D. E. Gaona, C. Jiang, and T. Long, "Highly efficient 11.1-kW wireless power transfer utilizing nanocrystalline ribbon cores," *IEEE Trans. Power Electron.*, vol. 36, no. 9, pp. 9955–9969, Sep. 2021.
- [13] X. Liu, C. Ma, E. Fan, L. Zhao, and Q. Ge, "A method for suppressing core eddy current loss caused by leakage flux in nanocrystalline high-frequency transformer," in *Proc. IEEE 6th Int. Elect. Energy Conf.*, 2023, pp. 4410–4413.
- [14] R. Kolano et al., "Amorphous soft magnetic core for the stator of the high-speed PMBLDC motor with half-open slots," *IEEE Trans. Magn.*, vol. 52, no. 6, Jun. 2016, Art. no. 2003005.
- [15] C. Dominguez-Palacios, J. Bernal, and M. M. Prats, "Characterization of common mode chokes at high frequencies with simple measurements," *IEEE Trans. Power Electron.*, vol. 33, no. 5, pp. 3975–3987, May 2018.
- [16] G. Calderon-Lopez, Y. Wang, and A. J. Forsyth, "Mitigation of gap losses in nanocrystalline tape-wound cores," *IEEE Trans. Power Electron.*, vol. 34, no. 5, pp. 4656–4664, May 2019.
- [17] S. Mukherjee, Y. Gao, and D. Maksimovic, "Reduction of AC winding losses due to fringing-field effects in high-frequency inductors with orthogonal air gaps," *IEEE Trans. Power Electron.*, vol. 36, no. 1, pp. 815–828, Jan. 2021.

- [18] X. Li, C. Jiang, H. Zhao, B. Wen, Y. Jiang, and T. Long, "Novel flexible nanocrystalline flake ribbons for high-frequency transformer design," in *Proc. IEEE Appl. Power Electron. Conf. Expo.*, 021, pp. 2891–2896.
- [19] Z. Luo, X. Li, C. Jiang, and T. Long, "Characterization of nanocrystalline flake ribbon for high frequency magnetic cores," *IEEE Trans. Power Electron.*, vol. 37, no. 12, pp. 14011–14016, Dec. 2022.
- [20] W. Zhang, Q. Yang, Y. Li, Z. Lin, M. Yang, and M. Mi, "Comprehensive analysis of nanocrystalline ribbon cores in high-power-density wireless power transfer pads for electric vehicles," *IEEE Trans. Magn.*, vol. 58, no. 2, Feb. 2022, Art. no. 8700605.
- [21] L. Wang, Z. Hu, Y.-F. Liu, Y. Pei, X. Yang, and Z. Wang, "A horizontal-winding multipermeability LTCC inductor for a low-profile hybrid DC/DC converter," *IEEE Trans. Power Electron.*, vol. 28, no. 9, pp. 4365–4375, Sep. 2013.
- [22] L. Wang, Y. Pei, X. Yang, Y. Qin, and Z. Wang, "Improving light and intermediate load efficiencies of buck converters with planar nonlinear inductors and variable on time control," *IEEE Trans. Power Electron.*, vol. 27, no. 1, pp. 342–353, Jan. 2012.
- [23] L. Wang, Z. Hu, Y.-F. Liu, Y. Pei, and X. Yang, "Multipermeability inductors for increasing the inductance and improving the efficiency of high-frequency DC/DC converters," *IEEE Trans. Power Electron.*, vol. 28, no. 9, pp. 4402–4413, Sep. 2013.
- [24] L. Liu et al., "Design and additive manufacturing of multi-permeability magnetic cores," in *Proc. IEEE Energy Convers. Congr. Expo.*, 2017, pp. 881–886.
- [25] J. Liu, Y. Mei, S. Lu, X. Li, and G.-Q. Lu, "Continuously variable multipermeability inductor for improving the efficiency of high-frequency DC–DC converter," *IEEE Trans. Power Electron.*, vol. 35, no. 1, pp. 826–834, Jan. 2020.
- [26] Y. Yoshizawa, S. Oguma, and K. Yamauchi, "New Fe-based soft magnetic alloys composed of ultrafine grain structure," *J. Appl. Phys.*, vol. 64, pp. 6044–6046, 1988.
- [27] G. Herzer, "Grain structure and magnetism of nanocrystalline ferromagnets," *IEEE Trans. Magn.*, vol. 25, no. 5, pp. 3327–3329, Sep. 1989.
- [28] E. A. Theisen, "Recent advances and remaining challenges in manufacturing of amorphous and nanocrystalline alloys," *IEEE Trans. Magn.*, vol. 58, no. 8, Aug. 2022, Art. no. 2001207.
- [29] H. M. LTD, Tokyo, Japan, *Nanocrystalline Soft Magnetic Material FINEMET* Vol. Brochure No. HL-FM10-D(PDF), 2016.
- [30] K. Byerly, Y. Krimer, C. Phatak, E. Theisen, and M. E. McHenry, "Magnetostrictive loss reduction through stress relief annealing in an FeNi-based metal amorphous nanocomposite," *J. Mater. Res.*, vol. 36, pp. 2843–2855, 2021.
- [31] M. K. Mu, Q. Li, D. J. Gilham, F. C. Lee, and K. D. T. Ngo, "New core loss measurement method for high-frequency magnetic materials," *IEEE Trans. Power Electron.*, vol. 29, no. 8, pp. 4374–4381, Aug. 2014.
- [32] W. A. Roshen, "Fringing field formulas and winding loss due to an air gap," *IEEE Trans. Magn.*, vol. 43, no. 8, pp. 3387–3394, Aug. 2007.
- [33] G. Bertotti, "General properties of power losses in soft ferromagnetic materials," *IEEE Trans. Magn.*, vol. 24, no. 1, pp. 621–630, Jan. 1988.
- [34] A. Boglietti, A. Cavagnino, M. Lazzari, and M. Pastorelli, "Predicting iron losses in soft magnetic materials with arbitrary voltage supply: An engineering approach," *IEEE Trans. Magn.*, vol. 39, no. 2, pp. 981–989, Mar. 2003.



Zhichao Luo (Member, IEE) received the B.S. degree in automotive engineering from the South China University of Technology, Guangzhou, China, in 2014, and the Ph.D. degree in automotive engineering from Tongji University, Shanghai, China, in 2019.

From 2019 to 2021, he was a Postdoctoral Fellow with the Department of Electrical and Computer Engineering, University of Toronto, Canada. From 2021 to 2023, he worked as a Postdoctoral Research Associate with the University of Cambridge, U.K. In 2023, he joined the School of Electric Power Engineering, South China University of Technology, Guangzhou, China, where he is currently an Associate Professor. He has also served as the industry liaison Chair of TC9: Wireless Power Transfer Systems in PELS. His current research interests include wireless power transfer technologies, high-frequency magnetic components, novel soft magnetic material, magnetic field modeling, and power electronics in electric vehicles.



Xinru Li (Student Member, IEEE) received the B.Eng. degree in materials science and engineering from the University of Science and Technology Beijing, Beijing, China, in 2017, and the M.Phil. degree in electrical engineering in 2019 from the University of Cambridge, Cambridge, U.K., where he is currently working toward the Ph.D. degree.

His research interests include magnetic materials, particularly for power electronics applications, wireless charging systems, and high-frequency transformers.



Chaoqiang Jiang (Member, IEEE) received the B.Eng. and M.Eng. degrees (first class Hons.) in electrical engineering and automation from Wuhan University, Wuhan, China, in 2012 and 2015, respectively, and the Ph.D. degree in electrical and electronic engineering from The University of Hong Kong, Hong Kong, in 2019.

He is currently an Assistant Professor with the Department of Electrical Engineering, faculty member in the State Key Laboratory of Terahertz and Millimeter Waves, City University of Hong Kong, Hong Kong. From 2019 to 2021, he was a Postdoctoral Research Associate with the University of Cambridge, Cambridge, U.K. Also, he has been affiliated with Clare Hall, University of Cambridge, since 2021. In 2019, he was a Visiting Researcher with the Nanyang Technological University, Singapore. His research interests include power electronics, wireless power transfer techniques, electric machines and drives, and electric vehicle technologies.

Dr. Jiang was the recipient of the CAPE Acorn Blue Sky Research Award at the University of Cambridge (Winner), and the First Prize in the Interdisciplinary Research Competition at the University of Hong Kong. He is currently an Associate Editor of *IET Renewable Power Generation*, Guest Editor of *Energies*, Guest Editor of IEEE OPEN JOURNAL OF VEHICULAR TECHNOLOGY.



Zongzhen Li received the Ph.D. degree in metallurgical engineering from the Central Iron & Steel Research Institute, Beijing, China, in 2014.

He is currently a Founder and Senior Engineer of Jiangsu JITRI Advanced Energy Materials Research Institute Company, Ltd., Changzhou, China. He has been involved in long-term research on the development of high-performance nanocrystalline soft magnetic materials and their industrialization technologies. He has currently authored and coauthored more than 40 research papers and more than 50 invention

patents.

Dr. Li was the Project Leader or Principle Investigator of more than 20 national research projects.



Teng Long (Member, IEEE) received the B.Eng. degree from the Huazhong University of Science and Technology, Wuhan, China, the B.Eng. (first-class Hons.) degree from the University of Birmingham, Birmingham, U.K., in 2009, and the Ph.D. degree from the University of Cambridge, Cambridge, U.K., in 2013.

Until 2016, he was a Power Electronics Engineer with the General Electric (GE) Power Conversion, Rugby, U.K. He is currently a Full Professor with the University of Cambridge. His research interests include power electronics, electrical machines, and machine drives.

Dr. Long is a Chartered Engineer (CEng) registered with the Engineering Council in the U.K.